Spatio-Temporal Scale Space Analysis of Photometric Signals with Tracking Error

Brien Flewelling*, Timothy S. Murphy †, Andrew P. Rhodes ‡,
Marcus J. Holzinger §, John A. Christian ¶

This paper will investigate the application of Scale-Space Theory, specifically Curvature Scale Space, to 1-Dimensional light curve signals generated by reducing imagery sequences taken from simulated telescopes tasked in various modes. As an observed object with a variable light curve is viewed from a sensor achieving a perfect rate track mode, there is a trade between the time fidelity of the reconstructed signal and integration time required to make accurate detections. As the tracking error increases, a sensor in a step-stare con-ops for example may trade spatial samples for intensity information as a function of time. This is commonly seen in streak observations of tumbling resident space objects. The method presented here will demonstrate how consistent light curves with maximum time resolution can be generated from observation sequences with variable tracking error, and sensor integration times. Additionally, the sparse representation of these signals using Curvature Scale-Space feature images will be investigated as a means for rapid correlation of light-curves against a large database. The proposed rapid correlations could be used to identify variable operating modes of a known object, or to identify an object as a member of a database using a method dependent on the order of the number of salient features as opposed to the number of observations.

I. Introduction

This paper aims to introduce two novel algorithms which, when combined enable robust analysis of electro-optical observations of Resident Space Objects (RSOs) observed in non-ideal scenarios. Space Situational Awareness can be described as the critical knowledge of the behavior of

*Research Aerospace Engineer, Space Vehicles Directorate, Air Force Research Laboratory, 3550 Aberdeen Ave. SE, Kirtland AFB, NM, USA

†Graduate Student, The Guggenheim School of Aerospace Engineering, Georgia Institute of Technology, North Ave NW, Atlanta, GA 30332

‡Graduate Student, Department of Mechanical and Aerospace Engineering, West Virginia University, Morgantown, West Virginia, 26506-6106

§Assistant Professor, The Guggenheim School of Aerospace Engineering, Georgia Institute of Technology, Atlanta, GA 30332

¶Assistant Professor, Department of Mechanical and Aerospace Engineering, West Virginia University, Morgantown, West Virginia, 26506-6106

objects in space. Historically data collected for astrometric measurements has supported the orbit determination process; a method by which one can predict the future translational behavior of an RSO. In contrast, photometric data collection supports the characterization of the RSO itself, to include space object size, mass, shape, spin-state, etc. Historical data collection modes also highlight the opposed nature of these two pieces of information. Astrometric observations are usually taken by a sensor tasked in rate track mode so that accurately localized observations of the stars can be used to derive an accurate astrometric reference against which observations of RSOs are measured.

Photometric observations are best performed when an excellent model for an RSOs motion is known and a rate-track mode is employed to ensure that each observation is made with favorable signal to noise ratio (SNR). This rate track motion causes the star signals to streak with the motion of the camera. Figure 1 shows an RSO in the same state observed in 1a rate track and 1b sidereal track modes. How divergent these two processes are depends on the difference in the required angular rate of the sensor needed for each mode. For example a ground sensor observing geostationary objects will see less of a difference between these modes (approx. 2 arcsec/sec) whereas a ground to low-earth orbit, or low earth orbit to geostationary observation would be significantly higher.

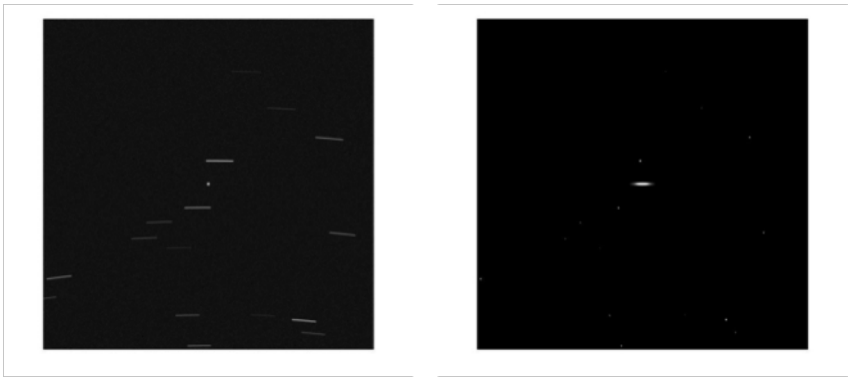

a) Object observed with perfect rate track. **b) Object observed with error in rate track.**

Figure 1. Different tracking modes and precision levels give different qualities of data for photometric analysis.

Tracking error resulting in the elongated appearance of an RSO in an image can happen for many reasons. The sensor could be inaccurately tasked, or not be capable of slewing at the required rate. It is also plausible that serendipitous observations occur while a sensor is tasked to observe another object. The method presented in Section II aims to enable autonomous photometric analysis of such signals with increasing apparent displacement in the sensor frame. It will be demonstrated that the approach to deriving multiple photometric observations from the signal is well behaved and avoids potential pitfalls of representing streaking, rotating RSOs as single values for each image. The method can be automatically cued for an RSO detection displaying an

eigenvalue ratio above a preset threshold or with discernable endpoints which indicate observed extension or displacement requiring advanced methods.

To account for the enhanced noise caused by deriving multiple photometric estimates from a single observation we present an application of Scale Space Analysis in Section III which enables a multi-scale representation of an RSOs light curve which is robust to noise. We explore this representation's ability to correctly characterize a light curve's deep structure in the presence of varying levels of noise and sampling. It is our intent that such a process enables effective comparisons of light curves taken by heterogeneous groups of sensors with different noise content and sampling rates.

Much work has been performed in the photometric analysis of space objects [1, 2, 3]. While many of these techniques perform very well for well-reduced image sets taken under favorable conditions, we intend for the combination of the tools presented in this work to apply to non-ideal data sets. This could include imagery collected from less stable, poorly localized, and more dynamic space or ground sensors. Further more, we intend to provide a potential means of extracting maximal information out of observations of opportunity. As space continues to become congested it is feasible that imagery could contain several RSOs with large variability in rates across a sensor frame. To derive useful astrometric and photometric information from these challenging image sets is the driver for this work.

II. Light Curve Sampling

A. Problem Motivation

Current state of the art light curve estimation focuses on rate tracking of objects and sufficiently long exposures to overcome noise. If a large exposure time is attempted on a dynamic light curve, this method can lead to factually incorrect data. As shown in figure 2, even without any noise, an inherent bias e exists, dependent on light curve curvature.

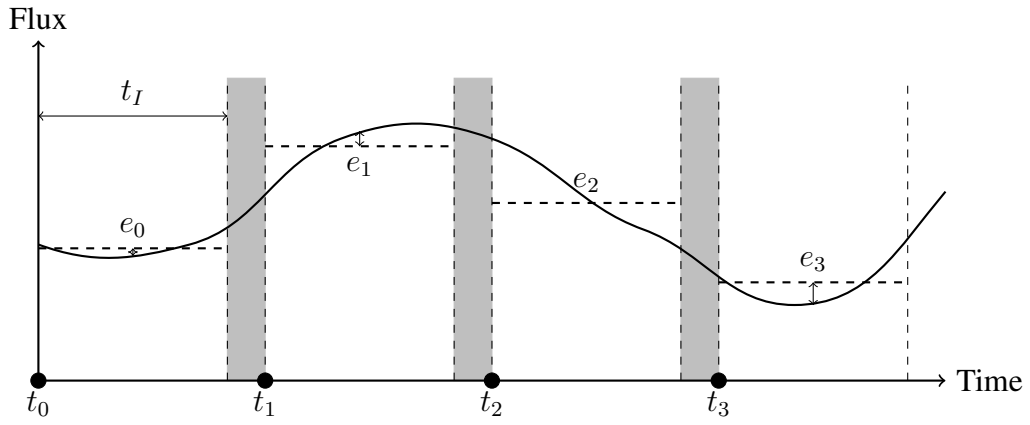

Figure 2. Four measurements on a variable magnitude light curve. Some measurements have no bias (2), while some have large biases (3).

The bias is dependent on curvature and is difficult to quantify without knowing the underlying signal. This can be solved by taking shorter exposures, but knowledge of required exposure is not always known before hand, leading to wasted or factually incorrect data. Actual flux measurements are computed as the average flux over the entire integration localized at the half integration time. When rate tracking is unavailable or contains significant error, streaking objects are treated as point objects. If objects streak through a frame, more temporally dense information should be available. This section will develop and test a method for sampling flux along the the streak of a RSO.

B. Theoretical Results

This subsection develops a method by which a streaking object with time dependent flux, $F(t)$, can be measured. $F(t)$ represents the average photons per second from the RSO being observed. These photons will actually arrive at a sensor randomly according to a Poisson distribution with $\lambda = F(t)$. This paper assumes that the read noise dominates the shot noise. Therefore, the read noise is representative of the noise in a given pixel, and the flux is not random.

Each photon is also localized by a random process modeled by an estimable distribution. The paper follows the convention of approximating the photon localization as a Gaussian distribution, shown in Equation 1 [4], [5].

$$g(\mathbf{x}) = \frac{1}{\sqrt{2\pi \det(\Sigma)}} \exp\left(\frac{-||(\mathbf{x}-\mathbf{x}_G)||^2}{2\det(\Sigma)^2}\right) \mathrm{d}t \tag{1}$$

where $\mathbf{x}_G$ is the mean of the localization Gaussian PDF, and Σ is the covariance matrix. Because the object is, by problem definition, streaking, the localization of the object also moves as a function of time. Figure 3 illustrates this fact.

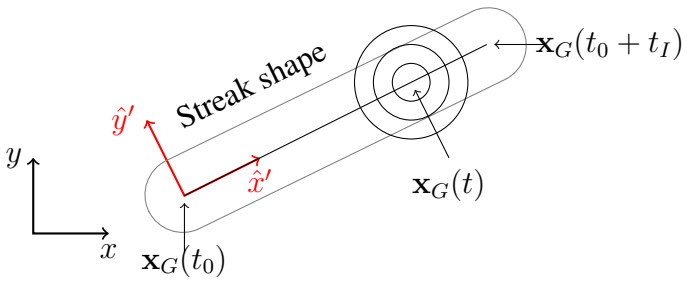

Figure 3. Gaussian evolving over time

The measured signal is the time integral of this Gaussian scaled by the flux.

$$f(\mathbf{x}) = \int_{t_0}^{t_0+t_I} F(t) \frac{1}{\sqrt{2\pi \det(\Sigma)}} \exp\left(\frac{-\|(\mathbf{x} - \mathbf{x}_G(t))\|^2}{2\det(\Sigma)^2}\right) \mathrm{d}t \tag{2}$$

This paper will assume the object has linear, non-accelerating dynamics, shown in Equation 3.

$$\mathbf{x}_G(t) = \mathbf{x}_G(t_0) + t\mathbf{v}, \quad t \in [t_0, t_0 + t_I] \tag{3}$$

Equation 2 is the density function for the number of photons in a given place in the sensor frame. The assumption is now made that the Gaussian is isotropic, it has equal standard deviations, so the axes can be rotated arbitrarily. This implies that, without loss of generality, equation 2 can be put into the orthogonal coordinates of $\hat{\mathbf{x}}'$ and $\hat{\mathbf{y}}'$ defined as

$$\hat{\mathbf{x}}' = \frac{\mathbf{v}}{\|\mathbf{v}\|}, \quad \hat{\mathbf{y}}' = \mathbf{R}(\pi/2)\hat{\mathbf{x}}' \tag{4}$$

where $\mathbf{R}(\pi/2)$ represents the rotation matrix to define a 90 degree rotation. Note that x' and y' will be used as the scalar variables along these coordinate axes. This is shown in figure 3, where $\hat{\mathbf{x}}'$ is always tangent to the path of $\mathbf{x}_G(t)$.

If the Gaussian is then integrated over the $\hat{\mathbf{y}}'$ axis, the Gaussian converges pointwise to a 1 degree of freedom Gaussian in the direction of the $\hat{\mathbf{x}}'$ axis as seen in equation 6.

$$f'(x') = \int_{-\infty}^{\infty} f(\mathbf{x}) \mathrm{d}y' \tag{5}$$

$$= \int_{-\infty}^{\infty} \int_{t_0}^{t_0+t_I} F(t) \frac{1}{\sqrt{2\pi \det(\Sigma)}} \exp\left(\frac{-\|(\mathbf{x} - \mathbf{x}_G(t))\|^2}{2\det(\Sigma)^2}\right) \mathrm{d}t \mathrm{d}y'$$

$$= \int_{t_0}^{t_0+t_I} F(t) \frac{1}{\sqrt{2\pi\sigma^2}} \exp\left(\frac{-(x' - x'_G(t))^2}{2\sigma^2}\right) \mathrm{d}t \tag{6}$$

Note that the coordinate x' is now a scalar defined along the $\hat{\mathbf{x}}'$ axis. The integration in time could now be explicitly calculated, if not for the unknown time varying flux. For times at which $|x'_G - x'| > 3\sigma$ the integrand will have effectively zero value. This allows the definition of a time interval, $[t_L(x'), t_U(x')]$, outside of which the integrand is effectively zero.

$$
\begin{aligned}
f'(x') &= \int_{t_0}^{t_0+t_I} F(t)\frac{1}{\sqrt{2\pi\sigma^2}}\exp\left(\frac{-(x'-x'_G(t))^2}{2\sigma^2}\right)\mathrm{d}t \\
&\approx \int_{t_L}^{t_U} F(t)\frac{1}{\sqrt{2\pi\sigma^2}}\exp\left(\frac{-(x'-x'_G(t))^2}{2\sigma^2}\right)\mathrm{d}t
\end{aligned} \tag{7}
$$

t_L and t_U are functions of x', and in practice are the times at which $|x'_G(t) - x'| = \pm 3\sigma$. Note that, the integral of the Gaussian will no longer evaluate to exactly 1, introducing a bias. This uncertainty is inherently tied to the fluctuation in $F(t)$, making this difficult to exactly calculate. $|x'_G(t) - x'|$ should be calculated along the path of $x'_G(t)$. In typical practice this should be close to a straight line. Finally, if $F(t)$ is assumed to be constant over the interval $[t_L, t_U]$, it can be pulled out of the integral which can then be explicitly calculated.

$$
\begin{aligned}
f'(x') &= \int_{t_L}^{t_U} F(t)\frac{1}{\sqrt{2\pi\sigma^2}}\exp\left(\frac{-(x'-x'_G(t))^2}{2\sigma^2}\right)\mathrm{d}t \\
&\approx F(x')\int_{t_L}^{t_U} \frac{1}{\sqrt{2\pi\sigma^2}}\exp\left(\frac{-(x'-x'_G(t))^2}{2\sigma^2}\right)\mathrm{d}t
\end{aligned} \tag{8}
$$

The dynamics in Equation 3 can be aligned with $\hat{\mathbf{x}}$ allowing a conversion between a spatial and temporal integral.

$$
\begin{aligned}
x'_G(t) &= x'_G(t_0) + t\|\mathbf{v}\| \\
\mathrm{d}x'_G &= \mathrm{d}t\|\mathbf{v}\|
\end{aligned} \tag{9}
$$

Combining Equations 8 and 9, where $v = \|\mathbf{v}\|$ gives the following

$$
\begin{aligned}
f'(x') &\approx F(x')\int_{x'_G-3\sigma}^{x'_G+3\sigma} \frac{1}{\sqrt{2\pi\sigma^2}}\exp\left(\frac{-(x'-x'_G)^2}{2\sigma^2}\right)v^{-1}\mathrm{d}x'_G \\
&= \frac{F(x')}{v}
\end{aligned} \tag{10}
$$

Also note that the flux is now expressed as a function of x', the position along the path of $\mathbf{x}_G$. The final product of this analysis, by combing and rearranging Equations 5 and 10, is

$$F(x') = v \int_{-\infty}^{\infty} \int_{t_0}^{t_0+t_I} F(t) \frac{1}{\sqrt{2\pi \det(\Sigma)}} \exp\left(\frac{-\|(\mathbf{x} - \mathbf{x}_G(t))\|^2}{2\det(\Sigma)^2}\right) \mathrm{d}t\mathrm{d}y'$$
$$= v \int_{-\infty}^{\infty} f(\mathbf{x})\mathrm{d}y' \tag{11}$$

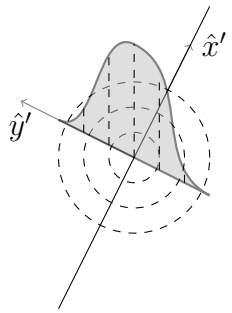

Figure 4. integration over the $\hat{y}'$ axis

The assumptions made in this derivation are detailed in Table B.

#	Assumption Details
1	Noise is dominated by read noise. Noise is normally distributed with a constant standard deviation in all pixels.
2	Point spread function can be represented as an isotropic Gaussian.
3	$F(t)$ is constant over some time interval $[t_L, t_U]$.
4	$\mathbf{x}_G(t)$ follows the linear dynamics in Equation 3.

C. Practical Implementation

The first step in calculating the flux is to define the trajectory that $\mathbf{x}_G$ has through the image. The results in this paper estimate it from the endpoints of the streak found via phase congruency corner detection [6]. Points, x', must be chosen along this trajectory to act as locations for sampling $F(t)$. This paper chooses points at intervals of 3σ of the localization Gaussian. More analysis should be done to define how fine this sampling can be without reporting redundant information.

First, the integral in Equation 11 cannot be evaluated over an infinite domain. Instead this must be approximated by integrating over the 3-sigma bounds of the Gaussian.

$$F(x') \approx v \int_{-3\sigma}^{3\sigma} f(\mathbf{x})\mathrm{d}y' \tag{12}$$

In reality, the signal $f(\mathbf{x})$ is not measured directly, but instead pixels are integrated over. The

measured pixel values represent the average function value over the pixel. The line over which the integral is evaluated intersects the pixels for varying lengths. Defining z_j as the pixel values over which the integral is evaluated, and l_j as the lengths over which the the y' axis intersects each pixel, the integral is estimated as

$$\begin{aligned} F(t) &= v \int_{-\infty}^{\infty} f(x) \mathrm{d}y' \\ &\approx v \sum_{j=1}^{M} z_j l_j \end{aligned} \tag{13}$$

D. Uncertainty Estimation

For the approximation in equation 13, uncertainties must be estimated. For each pixel i, there exist some signal component, s_i and some noise component, w_i.

$$z_i = s_i + w_i \tag{14}$$

$$w_i \sim \mathcal{N}(0, \sigma) \tag{15}$$

Note that this definition makes the assumption that background subtraction has occurred, allowing the noise to be modeled as zero mean. Moving forward under the assumption that σ approximates the noise for all pixels, there are N pixels used in a mean flux calculation, and noise between pixels is uncorrelated, the uncertainty can be quantified for the mean flux calculation.

$$\begin{aligned} F(t) &= \frac{1}{t_I} \sum_{i=1}^{N} z_i \\ \sigma_F &= \sqrt{\mathbb{E}[\frac{1}{t_I^2}[\sum_{i=1}^{N} z_i]^2]} \\ &= \frac{1}{t_I} \sqrt{\sum_{i=1}^{N} \mathbb{E}[z_i^2]} \\ &= \frac{\sqrt{N}\sigma}{t_I} \end{aligned} \tag{16}$$

For the sub-streak sampling method, Equation 13 must be considered a random variable, giving the following uncertainty.

$$
\begin{aligned}
F(t) &\approx v \sum_{j=1}^{M} z_j l_j \\
\sigma_F &= \sqrt{\mathbb{E}[v \sum_{j=1}^{M} z_j l_j]^2} \\
&= v \sqrt{\sum_{j=1}^{M} \mathbb{E}[z_j^2 l_j^2]} \\
&= v\sigma \sqrt{\sum_{j=1}^{M} l_j^2}
\end{aligned} \tag{17}
$$

E. Simulated Results

First, a simulation is run to demonstrate the existence of bias in mean flux measurements over variable flux signals. The underlying signal is a sinusoid with a frequency of $\omega = \frac{1}{45}$. Three exposures of ten seconds each are taken in a row, as part of an imperfect rate track tasking. Figure 6 shows the results from a simulation of a spacecraft with variable magnitude. The RSO has a flux signal dominated by a sinosoid with a 45 second period. The observer takes 10 second exposures for each of 3 consecutive intervals. A sample image from the simulated collection can be seen in Figure 5.

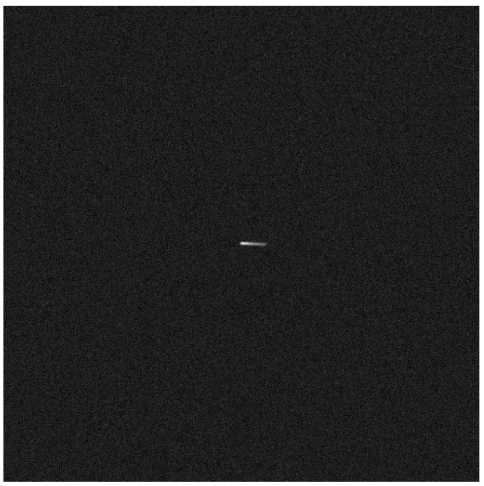

Figure 5. Simulated image of 10 second exposure observation of object with variable flux frequency of $\omega = \frac{1}{45}$

A mild noise presence of $\lambda = 9$ poisson noise is added to each pixel, approximated as a Gaussian. Background is estimated and subtracted prior to flux calculation, making the noise

nearly zero mean. The results of this simulation are shown in Figure 6. The first method in subplot (a) is a mean flux estimation calculated by summing the total photons over an entire streak and localizing it at the half integration time. When large curvature is present, this method demonstrates large bias as seen in subplot (c). This bias is due to the fact that the mean does not lie on the true signal when second order terms are significant. The new sub-sample method in subplot (b) is the equation 11 calculated at 4 evenly spaced points along the streak. Subplots (d) show the residuals and 3 sigma bounds for the sub-sample method. The mean flux sampling method has low associated uncertainties, but introduces significant bias for some measurements of this signal, due to reasons described in Section A. The uncertainty in the sub-sample method is larger, but shows significantly less bias. The sub-sample method also provides more data points and higher sampling density.

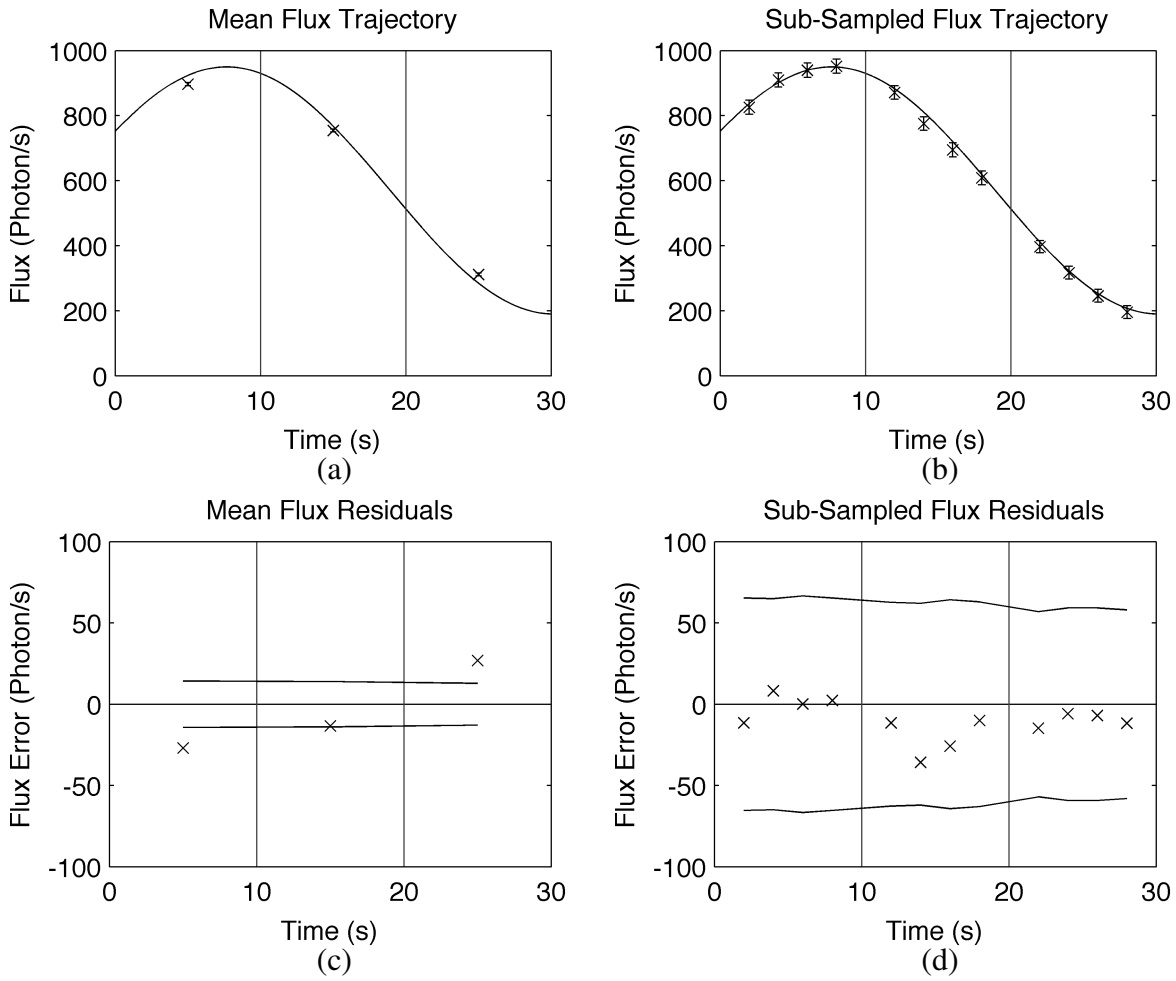

Figure 6. Photometry data for ten second exposure imperfect rate track. Sub-sample method shows more uncertainty, but provides more data points and mitigates inherent bias

A second simulation with a light curve composed of two sinusoids with different frequencies, phases, and amplitudes is shown now. The parameters of the two sines is shown in Table E.

	ω	ϕ	A
Signal 1	$\frac{1}{80}$	0	1
Signal 2	$\frac{1}{20}$	$\frac{-\pi}{2}$	0.5

The simulation is run over a variety of exposure rates. Tracking error is adjusted such that the sub-sample data always obtains the same number of data points. Results are shown in Figure 7, 8.

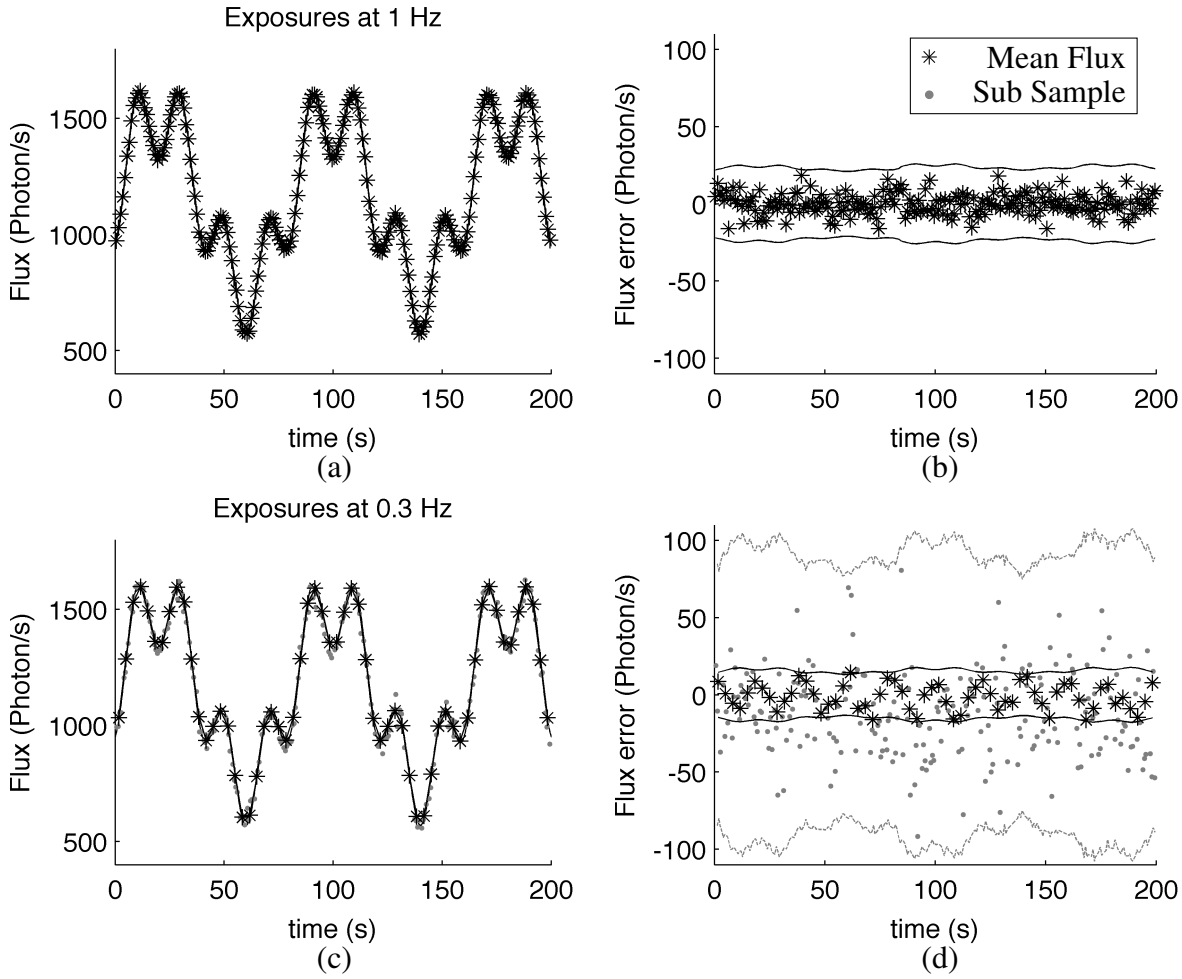

Figure 7. Two photometry collection methods compared over variety of sampling frequencies.

Figure 7(a,b) shows a sufficiently fast exposure rate. No under sampling problems happen and the curvature over an exposure does not cause significant error. Figure 7(c,d) shows exposure rate of 0.3 Hz, which starts to illustrate problems that can occur. A bias can be seen in the mean flux data points, that oscillates with the curvature of the signal. Out of the 60 data points, 3 fall outside of the expected 3-sigma bounds, illustrating the now non-Gaussian noise. The sub-sampled data points have significantly more noise, but has no bias and has well posed uncertainty.

Figure 8(a,b) shows exposure rate of 0.1 Hz, and shows significant advantages for the sub-sampling method. Note the 0.1 Hz is the Nyquist frequency for this light curve. The mean flux

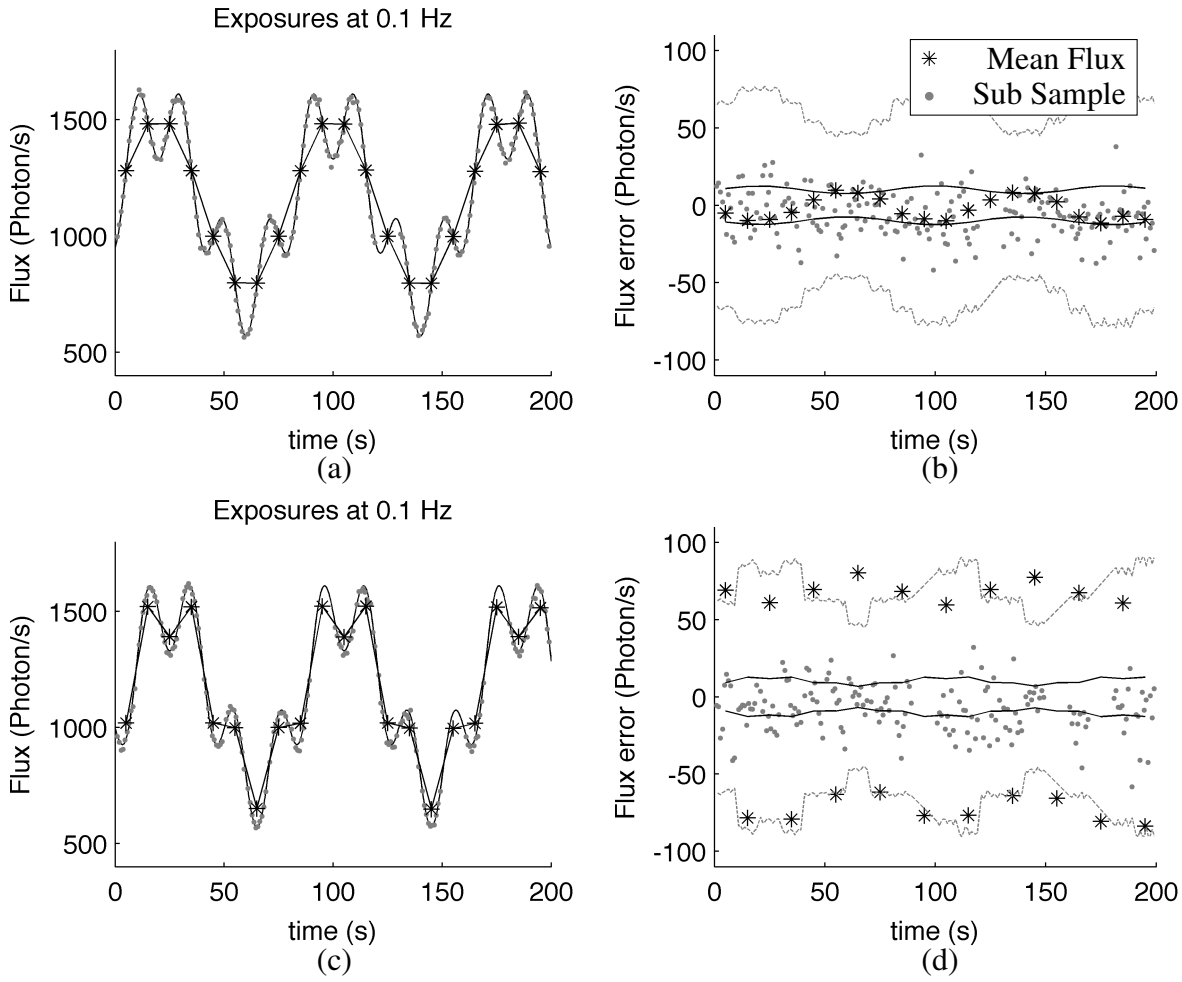

Figure 8. Two photometry collection methods compared over variety of sampling frequencies.

estimation method shows significant aliasing error as seen in (a). The high frequency component is not represented in the reconstructed signal when the mean flux method is used. In (b), an oscillating bias can be seen in the mean flux data. The sub-sample method is still invariant to changes in data types. Figure 8(c,d) also shows exposure rate of 0.1 Hz, but at a different phase. The new phase aligns the exposures with the maximum curvature. The error shown in (d) skyrockets compared to other test cases, because this is a worst case scenario.

The next section explores the application of curvature scale space to light curves with variations in noise content and sampling rate. We stress here that either method described in this section could be used to generate the realizations analyzed. CSS is demonstrated as a robust means to define a fingerprint which efficiently represents an object's light curve for purposes of database recall.

III. Scale Space Representation of Light Curves

A. Motivation

It is evident from Section II that we could easily encounter a sampling of the flux $F(t)$ at wildly varying resolutions, depending on the imager used, the apparent velocity of the object through the image, the integration time, and a host of other factors. The signal-to-noise ratio may also be quite poor. Together, these two factors introduce challenges in both characterizing salient features in an observed light curve as well as performing any type of reliable object identification.

We suggest that scale space theory — a field of study concerned with multi-scale signal representation [7, 8] — may be a powerful tool for interpreting light curve data. As a raw light curve signal is smoothed, we retain only features of lower frequency (larger scale). The result is that high frequency noise is eliminated and what remains approaches the underlying deep structure as the scale increases. There are numerous types of scale space representations [7, 8, 9, 10, 11], but we choose to focus on Curvature Scale Space (CSS) [12]. We do not assert that CSS is the best possible scale space method, but only that it is a suitable and representative technique for use as a proof of concept approach in the analysis of 1-D light curves.

As an example, Fig. 9a shows the evolution from top to bottom of how an oscillating curve is smoothed to its underlying straight line function. Fig. 9b depicts the same signal with significant noise also approaching the same basic structure. The CSS for these light curves is shown in Fig. 9c.

To our knowledge, the present work is the first application of scale space theory (and CSS, in particular) to the analysis of 1-D light curves. In addition to the novel use of CSS on 1-D light curves, a new algorithm was developed to better facilitate 1-D curve matching. The matching algorithm is completely described in Subsection D. Using this matching algorithm, this process successfully matches a sample CSS with various sampling frequency and noise levels against a catalog of other CSSIs.

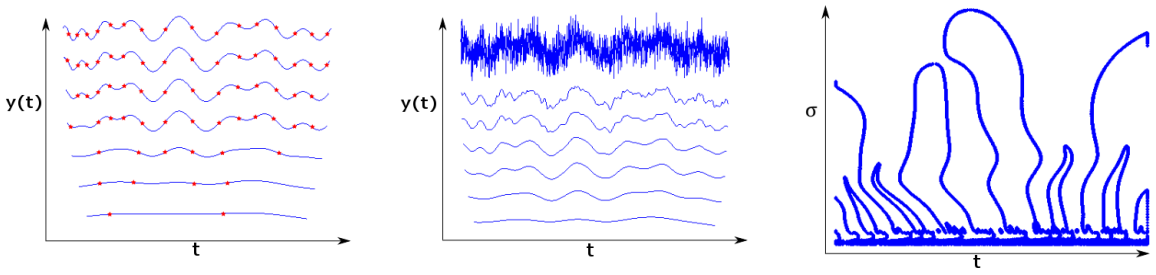

a) Light Curve evolution without noise showing inflections points that create the CSSI in plot c

b) Light curve evolution with significant noise

c) Curvature Scale Space Image (CSSI) of light curve

Figure 9. Multi-scale light curve evolution of a) and b) exhibit similar multi-scale evolution invariant of initial noise. c) Multiple peaks at small scales (σ) that represent noise, and few curves at large scales representing salient features. A curve corresponds to the evolution of the red stars in a).

B. Mathematical Background

The CSS Image (CSSI) of a curve is created by finding the points where the local curvature equals zero at varying levels of scale. These are locations along the curve where the curvature sign changes (inflection points). Though this method was originally developed for 2-D closed curves, its mathematical foundation holds for 1-D open curves. For the 1-D application to light curves, $x(t) = t$ is the sampling intervals of the light curve, and $y(t)$ is the flux.

To express the signal at increasing scales, we will convolve the raw signal with a Gaussian kernel of increasing width (standard deviation). Such a convolution is effectively a blurring process that acts as a low-pass filter, with a larger width having a lower cutoff frequency. Thus, we may express the signal at scale σ though a convolution of the form,

$$X\left(t,\sigma\right) = x\left(t\right) * g\left(t,\sigma\right) \tag{18}$$

$$Y\left(t,\sigma\right) = y\left(t\right) * g\left(t,\sigma\right) \tag{19}$$

where $*$ is the convolution operator and $g\left(t,\sigma\right)$ is the 1-D Gaussian kernel,

$$g\left(t,\sigma\right) = \frac{1}{\sqrt{2\pi\sigma^2}} \exp\left(-t^2/2\sigma^2\right) \tag{20}$$

As a result, by the definition of the convolution operator, we have the following expression for $X\left(t,\sigma\right)$

$$X\left(t,\sigma\right) = \int_{-\infty}^{\infty} x\left(\tau\right) \frac{1}{\sqrt{2\pi\sigma^2}} \exp\left(-\left(t-\tau\right)^2/2\sigma^2\right) \quad d\tau \tag{21}$$

along with a similar expression for $Y\left(t,\sigma\right)$.

Construction of the CSSI requires that we find the locations where curvature changes sign. Begin by defining the curvature at t and scale σ by

$$\kappa\left(t,\sigma\right)=\frac{\dot{X}\ddot{Y}-\dot{Y}\ddot{X}}{\left(\dot{X}^{2}+\dot{Y}^{2}\right)^{3/2}} \tag{22}$$

Because the both convolution and derivatives are linear operators, it is generally better to compute the first and second derivatives of X and Y by convolving x and y with the first and second derivatives of g, rather than by differentiating X and Y directly. That is, for X, we have

$$\begin{aligned}\dot{X}\left(t,\sigma\right)&=\frac{\partial X\left(t,\sigma\right)}{\partial t}=\frac{\partial\left[x\left(t\right)*g\left(t,\sigma\right)\right]}{\partial t}\\&=x\left(t\right)*\left(\frac{\partial g\left(t,\sigma\right)}{\partial t}\right)\end{aligned} \tag{23}$$

and

$$\ddot{X}\left(t,\sigma\right)=x\left(t\right)*\left(\frac{\partial^{2}g\left(t,\sigma\right)}{\partial t^{2}}\right). \tag{24}$$

Similar equations exist for $\dot{Y}$ and $\ddot{Y}$.

For the problem of interest here, where $x(t)=t$, the convolution of $x(t)$ with a Gaussian kernel may be evaluated directly as[a]

$$\begin{aligned}X(t)&=x(t)*g(t,\sigma)\\&=\frac{1}{\sqrt{2\pi\sigma^{2}}}\int_{-\infty}^{\infty}\tau\exp\left(-(t-\tau)^{2}/2\sigma^{2}\right)d\tau\\&=x(t)=t.\end{aligned} \tag{25}$$

With this in mind, the derivatives of X are $\dot{X}=c$, a constant, and $\ddot{X}=0$. Then Eq. 22 becomes

$$\kappa\left(t,\sigma\right)=\frac{c\ddot{Y}}{\left(c^{2}+\dot{Y}^{2}\right)^{3/2}} \tag{26}$$

and curvature becomes only a function of Y. Then curvature is found where the flux changes concavity.

The zero local curvature locations – inflection points – of the parameterized curve are found and recorded on a graph where the horizontal axis is the value of the path-length variable ζ and the vertical axis is the current σ, the width of the Guassian kernel. For small values of σ, the CSSI contains information about the noise. As the scale σ increases, the light curve becomes smoother,

[a]Where we make use of the identity $\int_{-\infty}^{\infty}x\exp\left\{-a(b-x)^{2}\right\}dx=b\sqrt{\pi/a}$, which may be found in any standard table of definite integrals for exponential functions.

and now the CSSI shows information about the curvature of the underlying signal structure. Each peak in the CSSI is the result of a peak-trough group of the original light curve. An example CSSI is shown in Fig. 9c which has many small peaks at low scale (corresponding to noise) and only a few distinct peaks at high scale (corresponding to distinct features of the light curve).

C. Application to 1-D Light Curves

Our desire to store multi-scale representations in a concise form led to the selection of curvature scale space. Since CSS was originally created to analyze 2-D object silhouettes and only briefly considers open curves, it generates a few interesting artifacts on 1-D light curves. In Fig. 9c, some of the CSS curves do not completely close, ending in mid-formation on the left and right boundaries. This occurs because the measured light curve is not closed and does not provide information of what happens after the end points. Some CSSIs will also have a single line traveling vertically through the scales that does not connect to make a closed CSS curve; this line is a remnant of the light curve centroid and that it is not closed.

In order to apply a matching algorithm to the light curve CSSIs, certain points must be identified for matching. Peaks in the CSSI correspond to locations of inflection points present in each scale of the light curve. The CSSI peaks are distinct markers for a measured light curve and may be recorded and matched. Peaks will not be found for any of the artifacts caused by CSS analysis on 1-D curves — which are easily found since they are the CSS curves that do not close (including those that terminate at graph boundaries).

Consider a light curve measured by various sensors, all with a different sampling frequency and noise levels. Table 1 shows how this light curve would appear with varying sampling frequency on the columns and varying standard deviation of measurement noise ν on the rows. The best given light curve is with $5\,Hz$ sampling frequency and a standard deviation of $\nu = 0$ noise. The worst given light curve is with $0.5\,Hz$ sampling frequency and standard deviation of $\nu = 100$ noise.

Now consider how the CSSI of these light curves vary in Tab. 2. All of the CSSIs exhibit a similar structure with a single prominent curve in the middle with a number of smaller curves of similar height. CSSIs with sampling frequencies of $1.25\,Hz$, $3\,Hz$, and $5\,Hz$ all contain one large curve and seven smaller curves. The CSSIs of sampling frequency $0.5\,Hz$ still show one large curve in the center but less than seven smaller curves. This discrepancy is due to the low sampling rate. While the CSSIs of sampling frequency $0.5\,Hz$ show slightly different curves than of the other sampling frequencies, this is not a failure of the curvature scale space representation technique, but a reminder that there is not sufficient information from the originally sampled light curve to distinguish all of the salient features.

Now focus on the column of sampling frequency $5\,Hz$ and how the CSSIs change with various noise levels. Remember that points of larger scale σ in the CSSI correspond to inflection points of the measured light curve and points of small scale σ are representative of the noise. Notice

	Sampling Frequency			
std. ν	0.5 Hz	1.25 Hz	3 Hz	5 Hz
0	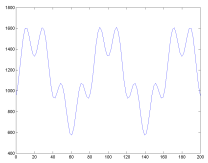	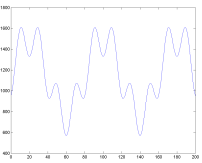	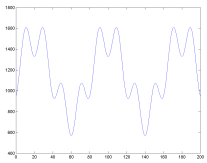	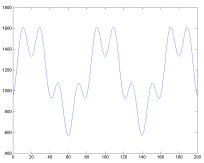
15	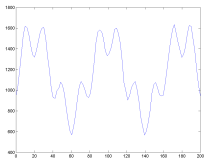	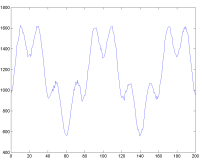	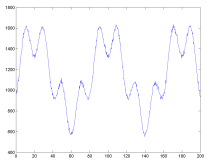	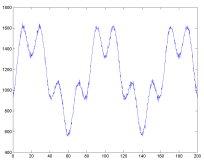
50	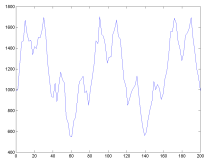	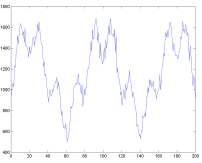	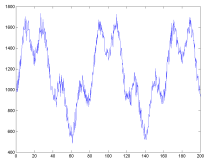	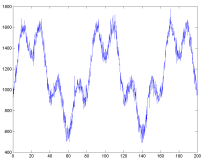
100	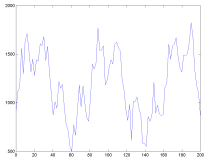	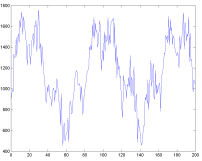	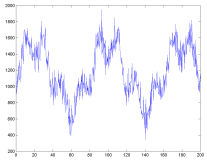	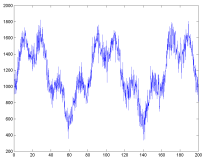

Table 1. A light curve with varying sampling frequency verse varying noise

how the prominent curves of the CSSIs remain similar while the noise level increases; there is only an increase in then number of curves of small scale which characterize an increase in noise. This shows that noise has a smaller effect on the CSSI than sampling frequency. Therefore, in combination with the previous paragraph, it is more important to have a densely sampled rather than a sparsely sampled light curve with noise affecting later more than the former. The technique shown in Section II provides these requirements.

D. Matching Results

We chose the CSS representation to describe a light curve because it reduces the signal to a few salient features — which may be used for the rapid matching of signals with drastically different resolution. For example, the light curve of Tab. 1 measured at $5\,Hz$ for 200 seconds generates 1000 points, while it's CSSI contains only 8 total points corresponding to the inflection points. Therefore, a curvature scale space database recall algorithm with 8 points is much faster than cross-correlation of the original light curve.

It is often important to compare the information contained within a newly observed light curve to observations in a database. We presend here how the information contained within a light curve's CSSI can be used to do this efficiently. This process will inform the user which model light

std. ν	Sampling Frequency 0.5 Hz	1.25 Hz	3 Hz	5 Hz
0	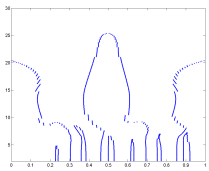	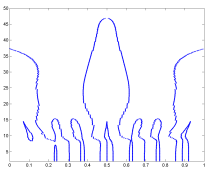	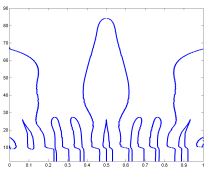	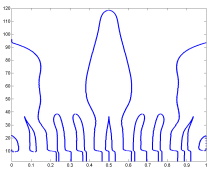
15	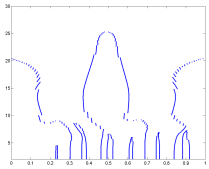	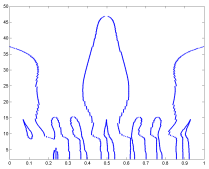	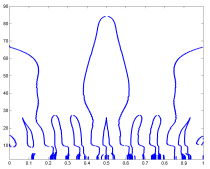	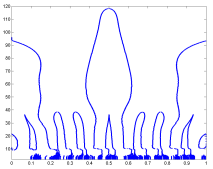
50	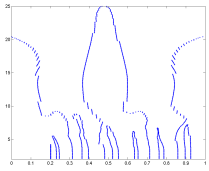	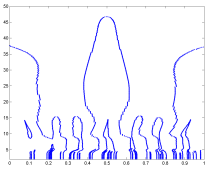	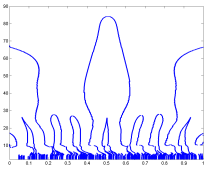	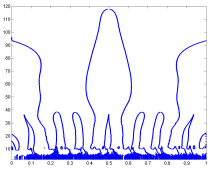
100	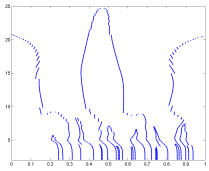	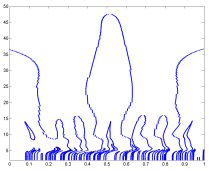	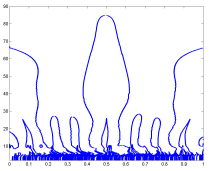	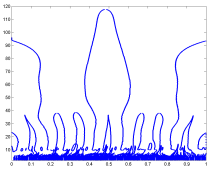

Table 2. CSS Images with varying sampling frequency verse varying noise of light curves of Tab. 1

curve from database is most representative of the observed light curve. The matching algorithm discussed here was adopted from [12] and modified to more efficiently handle 1-D signals. We acknowledge that components of this matching approach are heuristic in places, a topic we aim to address further in future work. As for now, this approach seems to produce adequate results for our proof-of-concept study.

Begin with the assumption that the observed light curve and the model light curves are of all the same duration. Normalize the time of each light curve such that the domain of the CSSIs exist on the interval $[0, 1]$. That is, define normalized time $\zeta = (t - t_0)/(t_{max} - t_0)$.

Further assume that there are g model CSSIs in the database. Let the k-th model light curve CSSI have m_k peaks defined by the set of 2-D points $\mathcal{M}_k = \{\mathbf{m}_{kj} | \mathbf{m}_{kj} = [\zeta_j, \sigma_j]\}_{j=1}^{m_k}$. Likewise, assume that the observed CSSI has n peaks defined by the set of 2-D points $\mathcal{O} = \{\mathbf{o}_i | \mathbf{o}_i = [\zeta_i, \sigma_i]\}_{i=1}^{n}$. We order the points in both $\mathcal{M}_k$ and $\mathcal{O}$ by scale with the largest scale feature is first, $\sigma_1 \geq \sigma_2 \geq \ldots \geq \sigma_n$.

Starting with these sets of observed and model CSSIs, the matching process is as follows:

1. Set $k = 1$ to begin with the first model CSSI.

2. Select the k-th model CSSI . For every point in $\mathcal{O}$, consecutively match it to each of the points

in $\mathcal{M}_k$ that are larger in scale than itself. For each match, calculate a scaling parameter κ that vertically scales the smaller maxima to the larger. Also calculate a shifting parameter α that shifts the smaller maxima left or right to the larger. Thus, each point in $\mathcal{O}$ will generate at most m_k parameter pairs $[\kappa, \alpha]$. Since there are n points in $\mathcal{O}$, there will be $s \leq nm_k$ total parameter pairs.

3. Apply each parameter pair $[\kappa, \alpha]$ to all the points in $\mathcal{O}$. This will generate s different scaled versions of $\mathcal{O}$, which we define as $\mathcal{O}'_z = \{\mathbf{o}'_{zi} | \mathbf{o}'_{zi} = [\zeta'_{zi}, \sigma'_{zi}]\}_{i=1}^{n}$, where $z = 1, \ldots, s$.

4. Now compute the value of the cost function, which we have customized for the matching of 1-D light curve CSSIs. A low cost is best and signifies a closer match. The cost for the comparison between each $\mathcal{O}'_z$ and $\mathcal{M}_k$ is generated as follows:

   - Define the set of scaled points in $\mathcal{O}'_z$ inside the domain $[0, 1]$ as $\hat{\mathcal{O}}'_z$ and those outside this domain as $\check{\mathcal{O}}'_z$. That is,

   $$\hat{\mathcal{O}}'_z = \{\mathbf{o}'_{zi} \in \mathcal{O}'_z : 0 \leq \zeta'_{zi} \leq 1\}$$

   $$\check{\mathcal{O}}'_z = \mathcal{O}'_z \setminus \hat{\mathcal{O}}'_z$$

   Only the points in $\hat{\mathcal{O}}'_z$ are considered for matching. Matching points in $\check{\mathcal{O}}'_z$ would promote partial CSSI overlap, but this approach penalizes partial overlaps and favors complete overlap matching of the CSSIs.

   - For each in point in $\hat{\mathcal{O}}'_z$ find the closest point in $\mathcal{M}_k$. Add the Euclidean distance between these points to the cost, and remove the matched points from their respective lists. Or, mathematically, for the first $p = \min\{n, m_k\}$ points iteratively apply the following:

   $$d_i = \underset{\mathbf{m}_{kj} \in \mathcal{M}_k^{(i)}}{\text{Minimize}} \|\hat{\mathbf{o}}'_{zi} - \mathbf{m}_{kj}\|$$

   $$\mathcal{M}_k^{(i+1)} = \mathcal{M}_k^{(i)} \backslash \{\mathbf{m}_{k\hat{j}}^{(i)}\}, \quad \text{where } \mathcal{M}_k^{(1)} = \mathcal{M}_k$$

   and where $\mathbf{m}_{k\hat{j}}^{(i)}$ is the model feature from $\mathcal{M}_k^{(i)}$ that minimizes the cost function for the i-th point.

   - When all the points in $\hat{\mathcal{O}}'_z$ or $\mathcal{M}_k$ have been matched – where one list is empty and the other still contains points – place the remaining points in the set $\mathcal{R}$. The points in $\mathcal{R}$ will also be added to the cost. This step penalizes the match when only a few of the

CSSI maximas match instead of all the maximas. That is,

$$\mathcal{R} = \left\{ \mathbf{r}_w | \mathbf{r}_w = \left\{ \begin{array}{ll} \{\hat{\mathbf{o}}'_{zi} \in \hat{\mathcal{O}}'_z : i > m_k\} & n > m_k \\ \mathcal{M}_k^{(n+1)} & n < m_k \\ \mathbf{0} & n = m_k \end{array} \right\} \right. \tag{27}$$

- Finally, we compute the cost (for the comparison of $\mathcal{O}'_z$ and $\mathcal{M}_k$) as

$$J_{kz} = \sum_{i=1}^{p} d_i + \sum_{\mathcal{R}} \|\mathbf{r}_w\| + \sum_{\check{\mathcal{O}}'_z} \|\check{\mathbf{o}}'_{zi}\|$$

5. After considering all of the s different scalings of $\mathcal{O}$, select the scaling $\mathcal{O}'_z$ and corresponding parameter pair $[\kappa, \alpha]$ that produce the lowest cost J_{kz}. Define the index for this scaling as $\hat{z}$, such that the cost of matching $\mathcal{O}$ with $\mathcal{M}_k$ is simply defined as $c_k = J_{k\hat{z}}$. Store the cost for this comparison in the set $\mathcal{C} = \{c_k\}_{k=1}^{g}$

6. It is desired to always scale up the smaller CSSI to prevent distortion from shrinking a CSSI. For this reason, repeat Steps 2–5 after switching the placement of $\mathcal{O}$ and $\mathcal{M}_k$. This accounts for that possibility that either the model or observed CSSI may be smaller than the other.

7. Repeat Steps 2–6 for $k = k + 1$ for all g models in the database. This will sequentially evaluate the observed CSSI against every model in the database.

8. The best match between the observed CSSI and the model CSSIs is now found by finding the index of the lowest cost in the set $\mathcal{C}$.

Two variables that have an effect on the matching algorithm, and thus the cost, are the sampling frequency and the noise level. First hold a constant noise level of $\nu = 0$ and vary the sampling frequency. The cost matrix for this self correlation is shown in Tab. 3 and shows how the sampling frequency affects the result of the matching algorithm. Auto-correlation of an exact match has the lowest cost of 0.0. While matching the $5\,Hz$ signal to the $0.5\,Hz$ signal has the largest, and relatively worst cost of 55.54, the cost value is only comparatively important to this table and does not reflect how the cost would evaluated when matched against various other light curves. Tab. 4 shows how varying the noise level while holding a constant $5\,Hz$ sampling rate. Noise affects the matching algorithm less than the sampling frequency. As long as the light curve is densely sampled, the level of noise has a small effect on the process of matching.

Now that there is a familiarity of the ranges of values the cost algorithm provides, it is necessary to match various instantiations of the model CSSI of Tab. 2 against a database to test the robustness of correctly identifying the same light curve. Utilize the row of $\nu = 0$ and the column of $5\,Hz$ from Tab. 2 naming them A through G as queried CSSIs to match against a database.

	Self-Correlation Matching Cost Matrix			
	0.5 Hz, ν 0	1.25 Hz, ν 0	3 Hz, ν 0	5 Hz, ν 0
0.5 Hz, ν 0	0.0	20.62	39.78	55.54
1.25 Hz, ν 0	20.62	0.0	13.94	19.67
3 Hz, ν 0	39.78	13.94	0.0	0.08
5 Hz, ν 0	55.54	19.67	0.08	0.0

Table 3. Cost of Matching Light Curve CSS Images. Variable Sampling Frequency, No Noise

	Self-Correlation Matching Cost Matrix			
	5 Hz, ν 0	5 Hz, ν 15	5 Hz, ν 50	5 Hz, ν 1000
5 Hz, ν 0	0.0	0.31	0.95	5.22
5 Hz, ν 15	0.52	0.70	0.61	4.70
5 Hz, ν 50	1.25	1.16	0.95	4.26
5 Hz, ν 100	2.05	2.11	1.95	4.64

Table 4. Cost of Matching Light Curve CSS Images. 5 Hz Sampling Frequency, Variable Noise

Apply the matching algorithm above to calculate a cost, remembering that the lower the cost, the better the match. Tab. 6 shows that the CSSI of the measured signal with various noise levels and sampling frequency (Signals A-G) correctly matches with the CSSI of Signal 1. The cost of matching the Signal A to Signal 6 is close to the lowest, occurring because the sampling frequency of Signal A is not sufficient to capture all the salient features of the measured light curve. Therefore, the CSSI matches close to incorrect signals because is shows some distortion and fewer closed curves than Signals D-G. Since the sampling frequency of Signal A is not sufficient to capture all salient features, it is appropriate that the matching cost for multiple curves is similar. When light curve sampling frequency is low, there may not be sufficient information measured to always correctly match to the correct signal, but there is enough information to give a short list of signals that are similar. It would be more accurate to say that the measured signal is similar to many model signals than to assume just one match.

IV. Conclusions

This paper introduced two novel algorithms which when combined enable robust analysis of photometric content of RSOs observed in non-ideal conditions. First, an approach to deriving multiple observations from a single streak contained in a long integration image of a tumbling RSO was explained and showed to be capable of providing well behaved estimates of photometric information in simulated imagery. At the cost of an increase in per-observation noise a light curve with higher temporal density than one point per frame is provided which can be used to prevent undesirable aliasing and bias effects. A scale space analysis of the resulting light curve was performed to determine if the curvature scale space could be a viable means to represent the multi-scale struc-

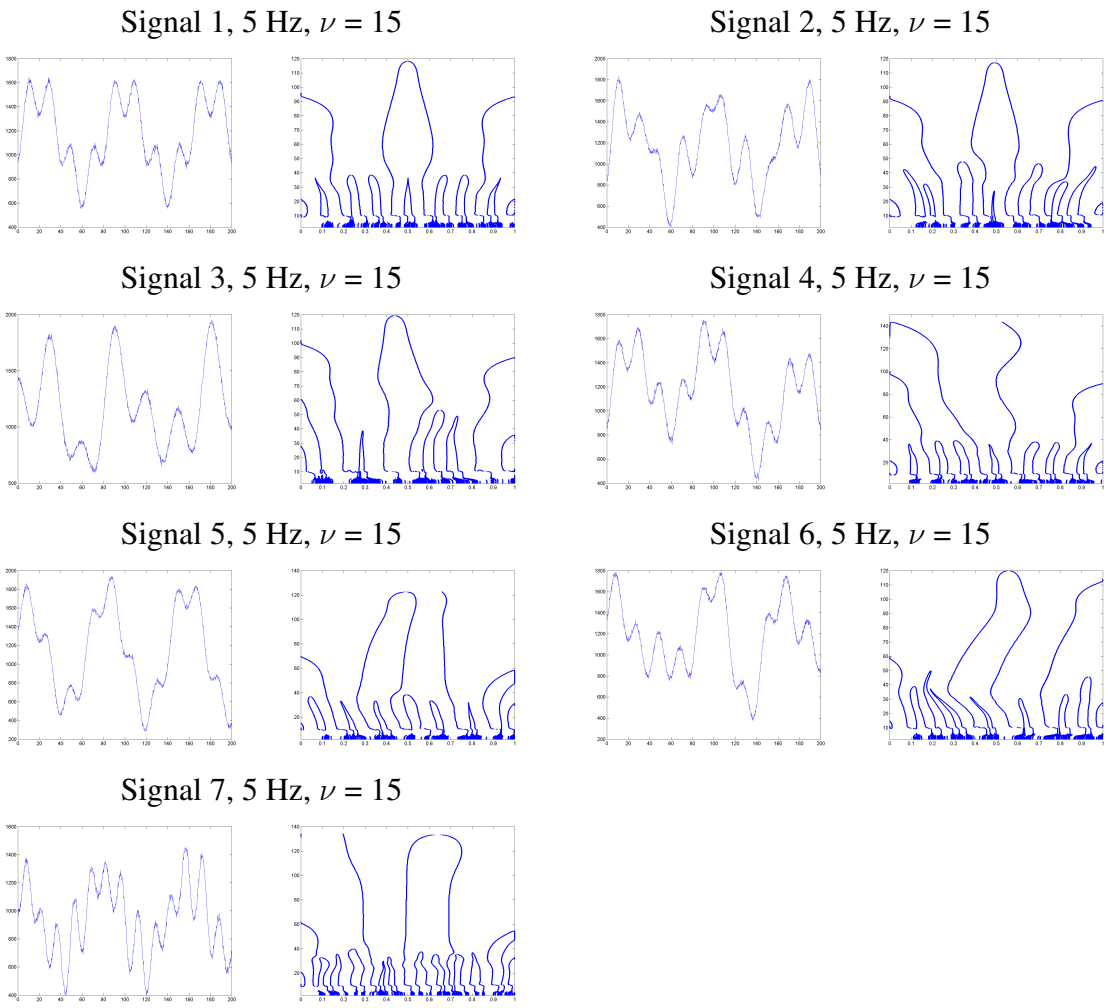

Table 5. Database of Signals and their CSSIs

Database Recall Cost Matrix							
	Signal A	Signal B	Signal C	Signal D	Signal E	Signal F	Signal G
Signal 1	**55.51**	**19.49**	**0.46**	**0.52**	**0.0**	**1.13**	**1.91**
Signal 2	75.16	71.59	53.75	44.53	44.70	44.97	45.31
Signal 3	173.43	192.55	173.91	173.85	174.05	174.18	175.16
Signal 4	168.25	228.10	397.21	121.53	121.33	121.45	121.47
Signal 5	76.80	86.94	66.66	66.60	67.21	67.91	66.95
Signal 6	58.08	59.76	40.69	40.61	40.91	44.09	115.36
Signal 7	144.06	155.04	173.40	173.33	173.84	175.34	174.03

Table 6. Signals A-G correctly match to Signal 1 for each case.

ture of observed light curves. It was demonstrated that in combination with a modified matching algorithm derived from [12] a simple example of data base recall and CCS stability in the presence of variations in sample rate and noise content is easily realized. Future work will focus on the detailed analysis of both techniques sensitivity to variations in real data as well as applicability to

large databases of light curves derived from various real-world observations. It is the vision of the authors that the rigorous combination of the tools presented here provide a means for effective data reduction of RSO observations in various challenging conditions including wide field of view sensors, fusion of various sensor observations, space base observations, and many other challenging applications.

V. Acknowledgments

The authors would like to thanks the Air Force Research Lab Scholars Program for funding this work. Support for Dr. Christian was made possible through the Air Force Office of Scientific Research (AFOSR) Young Investigator Program (YIP) through grant FA9550-15-1-0215.

References

[1] Sydney, P. F., Africano, J. L., Fredericks, A., Hamada, K. M., Hoo, V. S., Nishimoto, D. L., Kervin, P. W., Bisque, S., and Bisque, M., "Raven Automated Small Telescope Systems," *Proc. SPIE 4091, Imaging Technology and Telescopes, 237*, October 2000.

[2] Calef, B., Africano, J., Birge, B., Hall, D., and Kervin, P., "Photometric Signature Inversion," September 2006.

[3] Hall, D., Calef, B., Knox, K., Bolden, M., and Kervin, P., "Separating Attitude and Shape Effects for Non-resolved Objects," *The 2007 AMOS Technical Conference Proceedings*, 2007.

[4] RAO, U. V. G. and JAIN, V. K., "Gaussian and Exponential Approximations of the Modulation Transfer Function," *Journal of the Optical Society of America*, Vol. 57, No. 9, 1967, pp. 1159.

[5] JONES, R. C., "On the Point and Line Spread Functions of Photographic Images," *Journal of the Optical Society of America*, Vol. 48, No. 12, 1958, pp. 934.

[6] Kovesi, P., "Image features from phase congruency," *Videre: Journal of computer vision research*, Vol. 1, No. 3, 1999, pp. 1–26.

[7] Koenderink, J. J., "The Structure of Images," *Biological Cybernetics*, Vol. 50, August 1984, pp. 363–370.

[8] Babaud, J., Witkin, A. P., Baudin, M., and Duda, R. O., "Uniqueness of the Gaussian Kernel for Scale-Space Filtering," *IEEE Transactions on Pattern Analysis and Machine Intelligence*, Vol. PAMI-8, January 1986, pp. 26–33.

[9] Mackworth, A. and Mokhtarian, F., "The Renormalized Curvature Scale Space and the Evolution Properties of Planar Curves," *Computer Society Conference on Computer Vision and Pattern Recognition (CVPR)*, June 1988.

[10] Bangham, J. A., Chardaire, P., Pye, C. J., and Ling, P. D., "Multiscale Non-Linear Decomposition: The Sieve Decomposition Theorem," *IEEE Transactions on Pattern Analysis and Machine Intelligence*, Vol. 18, No. 4, 1996, pp. 529–538.

[11] Berrada, F., Aboutajdine, D., Ouatik, S. E., and Lachkar, A., "Review of 2D Shape Descriptors Based on the Curvature Scale Space Approach," *International Conference on Multimedia Computing and Systems*, April 2011, pp. 1–6.

[12] Mokhtarian, F. and Mackworth, A., "Scale-Based Description and Recognition of Planar Curves and Two-Dimensional Shapes," *IEEE Transactions on Pattern Analysis and Machine Intelligence*, Vol. 8, No. 1, January 1986, pp. 34–43.